Integrating Materials and Manufacturing Innovation
https://doi.org/10.1007/s40192-020-00182-4

TECHNICAL ARTICLE

ICME Framework for Simulation of Microstructure and Property Evolution During Gas Metal Arc Welding in DP980 Steel

M. J. Deepu[1] · **G. Phanikumar**[1]

Received: 28 July 2020 / Accepted: 14 August 2020

Abstract

An integrated computational materials engineering (ICME)-based workflow was adopted for the study of microstructure and property evolution at the heat-affected zone (HAZ) of gas metal arc-welded DP980 steel. The macroscale simulation of the welding process was performed with finite element method (FEM) implemented in Simufact Welding® software and was experimentally validated. The time–temperature profile at HAZ obtained from FEM simulation was physically simulated using Gleeble 3800® thermo-mechanical simulator with a dilatometer attachment. The resulting phase transformations and microstructure were studied experimentally. The austenite-to-ferrite and austenite-to-bainite transformations during cooling at HAZ were simulated using the Johnson–Mehl–Avrami–Kolmogorov (JMAK) equation implemented in JMatPro® software and with phase-field modeling implemented in Micress® software. The phase fractions and the phase transformation kinetics simulated by phase-field method agreed well with experiments. A single scaling factor introduced in JMatPro® software minimized the deviation between calculations and experiments. Asymptotic homogenization implemented in Homat® software was used to calculate the effective macroscale thermo-elastic properties from the phase-field simulated microstructure. FEM-based virtual uniaxial tensile test with Abaqus® software was used to calculate the effective macroscale flow curves from the phase-field simulated microstructure. The flow curve from virtual test simulation showed good agreement with the flow curve obtained with tensile test in Gleeble®. An ICME-based vertical integration workflow in two stages is proposed. With this ICME workflow, effective properties at the macroscale could be obtained by taking microstructure morphology and orientation into consideration.

Keywords Phase-field simulation · Dual-phase steel · Microstructure evolution · Welding · ICME · Vertical integration

Introduction

Integrated computational materials engineering (ICME) approach can help in reducing the cycle time for product development. Usage of physically based simulation in such an approach offers several interesting challenges such as taking microstructure into consideration while performing the macroscale simulation. Microstructure simulation is an important aspect in the ICME approach [1–3]. Microstructure simulation in steel involves simulation of simultaneous phase transformation such as the simultaneous transformation of austenite to ferrite, bainite, and martensite. These simulations are a major component of the vertical integration aspect of the ICME approach. Vertical integration aims at integrating simulations at different length scales and can help in consideration of microstructure information while performing macroscale finite element (FE) simulation [4, 5]. The currently available commercial FE simulation tools such as Simufact® and SYSWELD® use simplified approaches based on semiempirical models and rule of mixtures to predict the microstructure and corresponding properties. Rahul et al. [6] simulated welding in titanium alloy with finite element method and used physical simulation in Gleeble 3800® to simulate the heat-affected zone (HAZ) welding cycles. An integrated two-stage workflow was also proposed for accelerating the design of new alloys for weldability.

Phase-field modeling [7–9] is a powerful tool that uses diffuse interface approach [10] to simulate the various phase

---

✉ M. J. Deepu
mm14d207@smail.iitm.ac.in

G. Phanikumar
gphani@iitm.ac.in

[1] Department of Metallurgical and Materials Engineering, Indian Institute of Technology Madras, Chennai 600036, India

transformations in steels. Several studies have reported the phase-field simulation of austenite to ferrite [11–17] and austenite to bainite [18–21] transformation in steels. Ramazani et al. [22] studied the gas metal arc (GMA) welding in DP600 steel and also performed phase-field simulation of austenite-to-bainite transformation at HAZ during cooling. Toloui and Militzer [23] were the first to attempt the phase-field simulation of simultaneous formation of ferrite and bainite from austenite in steels.

Asymptotic homogenization [24, 25] is a powerful technique for the calculation of effective macroscale properties from phase-field simulated microstructure. Laschet et al. [26] simulated 3D microstructure of steels using phase-field method and performed thermo-elastic homogenization on the simulated microstructure. Laschet et al. [27] also simulated the forming process in pipeline steel and performed multiscale homogenization to calculate the effective properties for a representative volume element (RVE). Finite element method (FEM)-based virtual testing could be used for calculation of effective flow curve from an RVE [5]. Ramazani et al. [28] used FEM-based virtual test on 2D and 3D RVE in dual-phase (DP) steel to calculate the effective macroscale flow curve. A correlation was also proposed between flow curves obtained from 2D and 3D virtual test.

DP steels have gained importance in automotive industry in terms of lightweight. Several grades are being developed where the strength is increased while maintaining sufficient ductility. DP steels are produced by carefully controlled heat treatment [29, 30]. Hence, processing of DP steels is challenging as it involves phase transformations which affect the microstructure and final properties [5]. DP980 steel is one such grade that was chosen for this study. In the commercial DP steels category, only DP600 grade has been studied using phase-field simulations.

In the present work, the microstructure and property evolution at HAZ of GMA welding in DP980 steel were studied using an ICME-based methodology with an integrated usage of simulation tools and experimental methods. An experimentally validated FEM simulation of welding was used to obtain the thermal profile at HAZ of GMA-welded DP980 steel. With the obtained thermal profile, thermo-mechanical simulation was used for studying the microstructure at a point in the HAZ of GMA-welded DP980 steel. An ICME workflow in two stages is proposed. In the first stage of ICME workflow, semiempirical models implemented in JMatPro® software were used for microstructure and property calculations. Rule of mixture was used for calculation of effective macroscale properties from the calculated phase fractions and properties of individual phases. In the second stage, phase-field simulation was used for simulating the microstructure evolution at HAZ of GMA-welded DP980 steel. The simultaneous transformation of austenite to ferrite and austenite to bainite was simulated. Asymptotic homogenization and FEM-based virtual test were used for effective property calculation from the phase-field simulated microstructure.

Materials and Methods

Material

The material used for the present work was DP 980 steel with composition given in Table 1. The material was in the form of sheets of thickness 1.5 mm. The initial microstructure of the material was characterized with optical micrography, after tint etching with LePera reagent [31]. Figure 1 shows the initial microstructure of the material with ferrite, bainite, and martensite. On analysis of the microstructure, it was found that the material contains 60 ± 3% ferrite, 10 ± 2% bainite, and 30 ± 3% martensite.

Experimental Methods

GMA Welding

A bead-on-plate GMA welding was performed on DP980 steel sheet with a Fronius TPS 4000® power source. ER70S-6 electrode (AWS 5.18 standard) of 1.2 mm diameter with chemical composition given in Table 2 was used at a feed rate of 3.167×10^{-2} ms^{-1}. A K-type (Cr–Al) thermocouple was attached to the sample at a distance of 5 mm and

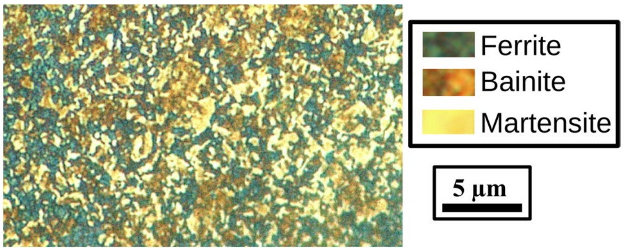

Fig. 1 Optical micrograph of DP980 steel used obtained after tint etching. Ferrite regions are indicated by blue color, bainite in brown, and martensite in yellow (in grayscale version of the image, darkest regions indicate ferrite, lightest regions indicate martensite, and the remaining regions indicate bainite)

Table 1 Material composition of DP 980 steel used for the study (wt%)

C	Mn	Si	Nb	Al	Cr	Ti	Ni	P	N	S	Fe
0.085	3.08	0.186	0.048	0.032	0.019	0.015	0.013	0.02	0.006	0.001	Bal.

Table 2 Chemical composition of ER70S-6 electrode used (wt %)

C	Mn	Si	Cu	Cr	Ni	Mo	P	S	V	Fe
0.15	1.85	1.15	0.5	0.15	0.15	0.15	0.025	0.035	0.03	Bal.

10 mm from weld center, for temperature measurement. An Ar + CO_2 mixture was used as the shielding gas. The electrode tip-to-work distance was set as 8 mm, and the welding was carried out at a speed of 6.67×10^{-3} ms^{-1}. The welding current and voltage were measured using an oscilloscope. Microhardness measurements were performed on polished sample by using a microhardness tester with a load of 500 gf and a dwell time of 10 s.

Physical Simulation of Thermal Profile at HAZ of DP980 GMA Weld

A thermal cycle simulation with Gleeble 3800® thermo-mechanical simulator was used to study the microstructure evolution during cooling part of the time–temperature profile at HAZ of DP980 GMA weld. Austenitization was assumed to be complete while heating at this point in HAZ. A standard geometry shown in Fig. 2 was used for dilatometry test in Gleeble 3800® thermo-mechanical simulator. To ensure full austenitization during the thermo-mechanical simulation, the sample was heated to a temperature of 1193 K at a heating rate of 20 Ks^{-1} and was held at that temperature for 300 s. It was subsequently cooled to room temperature, following the time–temperature profile at HAZ obtained from FEM simulation of welding. A control thermocouple was attached to the geometric center of the sample. A dilatometer was attached to the sample along the line where thermocouple was attached, to measure the dimension changes in the sample due to phase transformation during cooling.

Microstructure Characterization

The microstructure of material after thermal cycle simulation was characterized with optical microscope and scanning electron microscope (SEM). For characterization with SEM, the sample was etched with a 2% nital solution for 10 s. For optical micrography, the samples were etched with LePera reagent comprising 4 g of picric acid mixed with 100 ml of ethanol and 1 g of sodium bisulfide mixed with 100 ml distilled water for 15–20 s. The phase fraction of microstructural components was analyzed using image analysis in ImageJ® software [32]. The average grain size of ferrite grains was measured with linear intercept method (ASTM E 112 standard).

Tensile Test

A tensile test was performed on the material at room temperature at 0.01 s^{-1} strain rate, after heat treatment in Gleeble 3800® thermo-mechanical simulator. The sample was heated to 1193 K at a heating rate of 20 Ks^{-1} and was held at that temperature for 300 s. It was subsequently cooled to the designated temperature for tensile test. The time–temperature profile at HAZ of GMA-welded DP980 steel, obtained from thermal cycle simulation, was followed while cooling. An ASTM E8 standard reduced dimension sample with a gauge length of 25 mm [33] was used for the tensile test.

Simulation Methods

Finite Element Simulation of Welding

GMA welding in DP980 steel was simulated with FEM implemented in commercial software Simufact Welding® [34]. Local mesh refinement was applied in the weld area. Tetrahedral mesh was used with a mesh size of 0.375 mm up to a distance of 13 mm from the weld center line. Input material properties were obtained from JMatPro® software, assuming the material to be homogeneous. A Goldak double-ellipsoidal heat source [35] was used for the simulation. The simulation was performed for a current of 90 A and a voltage of 16.23 V, which were measured from GMA welding experiment, using a digital oscilloscope. The simulation took 3 h on 4 threads with an Intel Xeon® E5-2630 processor. Table 3 shows the parameters used for the welding

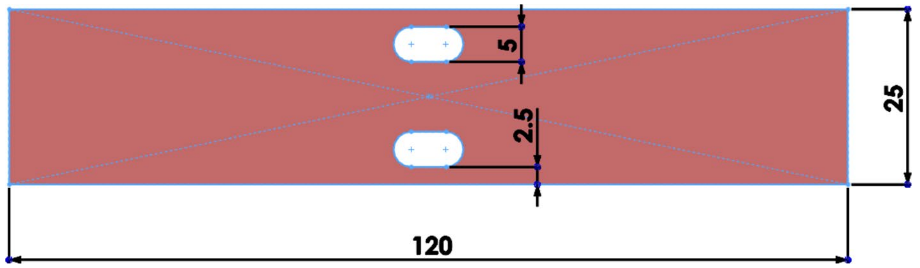

Fig. 2 Schematic diagram showing the dimensions of the sample used for thermal cycle simulation in Gleeble 3800® with dilatometer attachment (all dimensions in mm)

Table 3 Parameters used for FEM simulation of welding in Simufact Welding® software

Parameter	Value
Front length $\left(a_f\right)$	3.50 mm
Rear length $\left(a_r\right)$	7.60 mm
Depth (d)	3.23 mm
Width (b)	3.17 mm
Gaussian parameter (M)	3
Efficiency (η)	0.95
Convective heat transfer coefficient (h)	$20\,\mathrm{Wm^{-2}K^{-1}}$
Contact heat transfer coefficient (α)	$1000\,\mathrm{Wm^{-2}K^{-1}}$
Emissivity (ϵ)	0.6

simulation. The heat source parameters were calibrated based on the experimentally observed weld pool dimensions.

Phase Transformation Kinetics with JMAK Equation

JMatPro® software can provide a quick estimate of the phase fractions in the material microstructure after heat treatment, with a semiempirical approach. The JMAK (Johnson–Mehl–Avrami–Kolmogorov) equation implemented in JMatPro® software [36] was used for the simulation of phase transformations during cooling cycle at HAZ of GMA-welded DP980 steel. The experimentally measured prior austenite grain size of 5.4 μm after 300 s of holding at the austenitization temperature of 1193 K was used as an input for JMatPro® software.

Phase-Field Simulation

Multi phase-field method implemented in the commercial software Micress® was used for performing the phase-field simulations. The simultaneous transformation of austenite to ferrite and austenite to bainite during cooling was simulated. For the simulation of bainite formation, it was assumed that bainite formation occurs completely by diffusion. The bainite sheaves were considered as a single unit, without consideration of carbides, as the consideration of carbides will make the simulation computationally expensive. Concentration-coupled 2D phase-field simulations were performed on a domain size of 40 μm × 40 μm with a grid size of 0.1 μm. Fully austenite initial microstructure for the simulation was generated with Voronoi Tessellation using the prior austenite grain size of 5.4 μm measured from experiments. A constant composition was assumed in the initial microstructure. Random orientation was assigned to the grains. The thermodynamic data were obtained by live coupling with Thermo-Calc® database TCFE9. For the simulation of austenite-to-ferrite transformation, the diffusion data were obtained by coupling with Thermo-Calc® MOBFE4 database. For the simulation of austenite-to-bainite transformation, the diffusion coefficients were taken from the literature [18]. For the phase-field simulations, the material was considered to be a quaternary alloy with the components Fe, C, Mn, and Si. Local equilibrium negligible partitioning (LENP) assumption was used as the elemental redistribution criteria. Ferrite phase was assumed to nucleate only at triple junctions and grain boundaries of austenite phase. Bainite was assumed to nucleate randomly at the grain boundaries and in the bulk of austenite phase. Unlimited number of seeds were provided at the nucleation sites with shield distance and shield time as the controlling parameters. Interface mobility was considered as temperature dependent, according to Eq. 1, where μ_0 represents the pre-factor for interface mobility, Q is the activation energy, R is the gas constant, and T is the temperature in Kelvin. The pre-factor for interfacial mobility was used as a tunable parameter.

$$\mu = \mu_0 \exp\left(\frac{-Q}{RT}\right) \tag{1}$$

Interfacial energy and interface mobility for bainite were considered to be anisotropic according to Eq. 2 and Eq. 3, respectively, where $\vec{n}$ represents the interface normal vector [34]. Anisotropy function for interfacial energy is given by Eq. 4, and that for interfacial mobility is given by Eq. 5, n_x, n_y, and n_z represent the x, y, and z coordinates, $\sigma_0^{B\gamma}$ is the interfacial energy pre-factor, and $\mu_0^{B\gamma}$ is the interfacial mobility pre-factor [37]. In phase-field simulation, the interfacial mobility is kept as a tunable parameter to bring the capability of simulating all types of phase transformation, including the mixed-mode phase transformations. When the interfacial mobility is considered as temperature-dependent, the interfacial mobility pre-factor is used as the tunable parameter [13, 37]. The anisotropy factors δ_1^{μ}, δ_1^{σ}, and δ_2^{σ} were used for tuning the bainite sheaf morphology. Periodic boundary condition was applied in all directions.

$$\sigma^{B\gamma}\left(\vec{n}\right) = \sigma_0^{B\gamma} a^{\sigma}\left(\vec{n}\right) \tag{2}$$

$$\mu^{B\gamma}\left(\vec{n}\right) = \mu_0^{B\gamma} a^{\mu}\left(\vec{n}\right) \tag{3}$$

$$a^{\sigma}\left(\vec{n}\right) = \left[1 \pm 4\delta_1^{\sigma}\left(n_x^4 + n_y^4 + n_z^4 - 0.75\right)\right]\left(1 - n_z^2 - \delta_2^{\sigma} n_z^2\right) \tag{4}$$

$$a^{\mu}\left(\vec{n}\right) = \left[1 \pm 4\delta_1^{\mu}\left(n_x^4 + n_y^4 + n_z^4 - 0.75\right)\right]\left(1 - n_z^2 - \delta_2^{\mu} n_z^2\right) \tag{5}$$

For the concentration-coupled phase-field simulations in Micress software, Virtual EDX was performed along different lines in the simulated microstructure. The Virtual EDX scan gives the distribution of concentration of alloying elements across the line along which scanning is performed.

Table 4 shows some of the main parameters used for the phase-field simulation. The simulation took about 15 min using 8 threads on an Intel Xeon® E5-2630 CPU.

Virtual Tensile Test

Finite element-based virtual test was used to simulate the macroscale effective flow curve from the phase-field simulated microstructure. The remaining austenite was assumed to completely transform to martensite upon reaching room temperature. The phase-field simulated microstructure was considered as the representative volume element (RVE) and was meshed with 8-node brick element with reduced integration (C3D8R) with a mesh size of 0.1 µm. One element thickness was considered in the third dimension. Periodic boundary conditions were applied in all directions. A uniaxial tensile test was performed on this microstructure with finite element method implemented in Abaqus® software, at room temperature and a strain rate of 0.01 s^{-1}. Mesh2Abaqus® [38] code was used for writing the input files for Abaqus® software. The properties of microstructure constituents, namely ferrite, bainite, and martensite, were obtained from JMatPro® software for a prior austenite grain size of 5.4 µm, which was measured from experiments. The simulation took over an hour using a single thread on an Intel Xeon® E5-2630 CPU.

Asymptotic Homogenization

Asymptotic homogenization implemented in the commercial software Homat® [38] was used for obtaining the effective thermo-elastic properties from the phase-field simulated microstructure. The phase-field simulated microstructure was meshed using hexahedral brick element with one element thickness in the third dimension. The material input data for asymptotic homogenization were obtained from JMatPro® software for a prior austenite grain size of 5.4 µm, which was measured from experiments.

Results and Discussion

FEM Simulation of Welding

The temperature distribution during welding was studied using FEM simulation. The time–temperature profile measured from GMA welding experiments using thermocouple was compared with the simulated time–temperature profile at the corresponding point, at steady state. Figure 3a shows the comparison of time–temperature profile between simulation and experiment. ‘t1’ refers to thermocouple placed at a distance of 5 mm from the weld center line, and ‘t2’ refers to thermocouple that was placed at a distance of 10 mm from the weld center line. The agreement between simulated and experimental time–temperature profiles was satisfactory. The simulated weld bead geometry was compared with experimentally observed geometry with the help of weld macro image. Figure 3b shows the comparison between simulated and experimentally observed weld bead geometry. The left-hand side of Fig. 3b shows simulated weld bead where the color map refers to the temperature. The right-hand side of Fig. 3b shows a macro image of weld bead after bead-on-plate GMA welding in DP980 steel sheet. Figure 3c shows the hardness variation across the welded sample. The

Table 4 Parameters used for phase-field simulation

Parameter	Value
Shield distance (ferrite nucleation at triple junction)	6 µm
Shield distance (ferrite nucleation at grain boundary)	10 µm
Shield distance (bainite nucleation at grain boundary)	1.8 µm
Shield distance (bainite nucleation inside austenite grain)	3 µm
Shield time for ferrite	1 s
Shield time for bainite	2 s
Interfacial energy	$0.5\,\mathrm{Jm}^{-2}$
μ_0 (Austenite–ferrite)	$1 \times 10^{-6}\ \mathrm{m^4J^{-1}s^{-1}}$
μ_0 (Austenite–bainite)	$3.50 \times 10^{-9}\ \mathrm{m^4J^{-1}s^{-1}}$
δ_1^{μ}	0.5
δ_1^{σ}	0.1
δ_2^{σ}	0.5
δ_2^{μ}	0.05
Diffusion coefficient (carbon in bainite)	$5.84 \times 10^{-7}\mathrm{cm^2s^{-1}}$
Diffusion coefficient (manganese in bainite)	$3.58 \times 10^{-12}\mathrm{cm^2s^{-1}}$
Diffusion coefficient (silicon in bainite)	$1.19 \times 10^{-12}\mathrm{cm^2s^{-1}}$
Interface width	3 cells

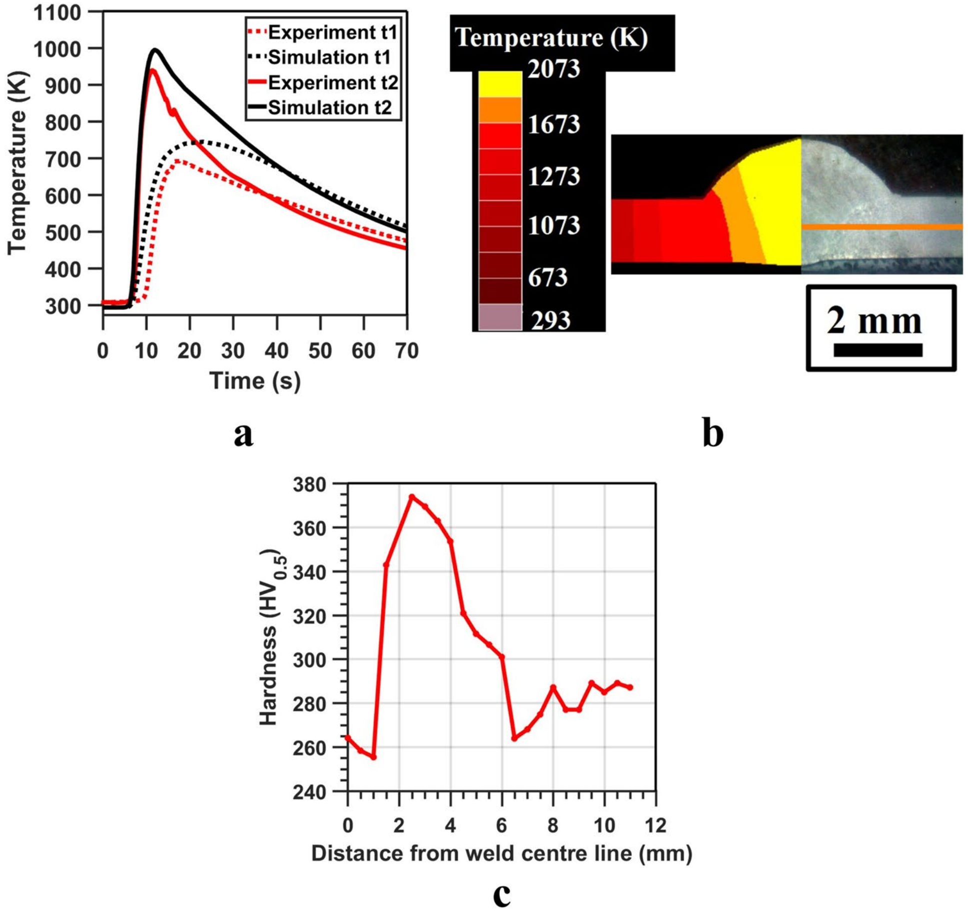

Fig. 3 **a** Comparison between simulated and experimental time–temperature profile during GMA welding of DP980 steel. 't1' refers to thermocouple placed at a distance of 5 mm from the weld center line, and 't2' refers to thermocouple that was placed at a distance of 10 mm from the weld center line. **b.** Comparison between simulated and experimental weld bead profile. The left-hand side of the image shows simulated weld bead where the color map refers to the temperature. The right-hand side shows a macro image of weld bead after bead-on-plate GMA welding in DP980 steel sheet. **c.** Hardness variation across the GMA-welded DP980 steel sample

weld regions were identified from the hardness variation. Figure 3b shows the line along which the microhardness measurements were taken.

Thermo-Mechanical Simulation of Thermal Profile at HAZ of DP980 GMA Weld and Microstructure Characterization

The time–temperature profile at HAZ of DP980 GMA weld was obtained from FEM simulation of welding. The microstructure evolution in the material during this thermal cycle was simulated in DP980 steel using physical simulation. Figure 4a shows the comparison between the time–temperature profile obtained from FEM simulation at a distance of 4.4 mm from the weld center line and the time–temperature profile measured from the sample using thermocouple, during the thermo-mechanical simulation. The time–temperature profile obtained from the FEM simulation closely followed those observed in the experiment. Figure 4b shows the optical micrograph of the sample after tint etching. Blue color indicates the ferrite region, dark brown represents bainite, and yellow/white indicates martensite. (In grayscale version of the image, darkest regions indicate ferrite, lightest regions indicate martensite, and the remaining regions indicate bainite.) Figure 4c shows the SEM SE image of the material microstructure after etching. The microstructure components were qualitatively identified from the microstructure to be ferrite (F), bainite (B), and martensite (M).

Phase Transformation Simulation and Effective Properties with JMatPro® Software

For the simulation of phase transformation at HAZ of GMA-welded DP980 steel, the time–temperature profile shown in Fig. 4a was used as an input to JMatPro® software. A scaling factor was introduced for ferrite and bainite to account for any deviation in the simulated result with experiments. Table 5 shows the phase area % of ferrite, bainite and martensite at HAZ of GMA-welded DP980 steel, calculated with JMatPro® software, with and without the use of scaling factor. Without any scaling factor, the simulated phase fraction deviated from experiments. The scaling factor (ratio) used in the current work was 0.4 for ferrite and 17 for bainite. These scaling factors shifted the time–temperature–transformation (TTT) curve of ferrite to the left and that of bainite to the right of the TTT diagram. Once the scaling factors were calibrated, the simulated results agreed well with experiments and could be used for parametric study.

The properties of individual phases were obtained from JMatPro® software using the built-in semiempirical models. Rule of mixture was used to calculate the effective macroscale properties with the help of phase fraction obtained with scaling factor and properties of individual phases. Table 6 shows the properties of ferrite, bainite, and martensite and the effective macroscale properties obtained using rule of mixtures.

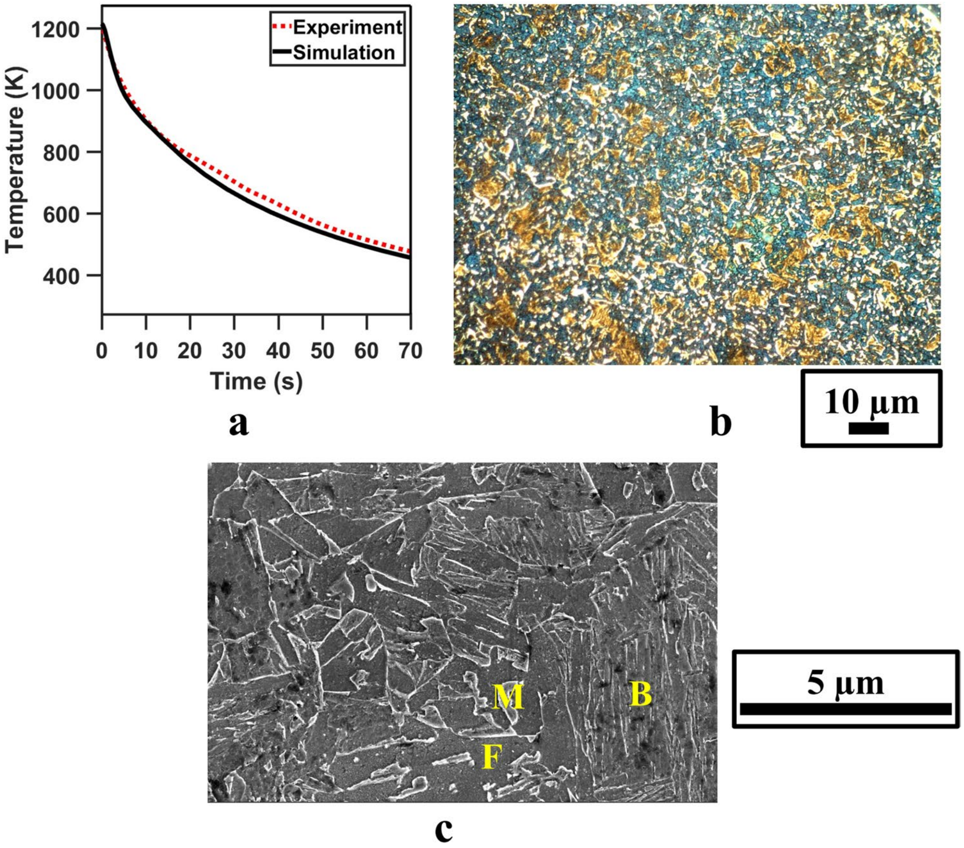

Fig. 4 Thermo-mechanical simulation of thermal profile at HAZ: **a.** Comparison between time–temperature profile obtained at HAZ of DP980 GMA weld, from FEM simulation and that followed by the thermo-mechanical simulation. **b.** Optical micrograph of material microstructure after thermo-mechanical simulation, obtained after tint etching. Blue color indicates the ferrite region, dark brown represents bainite, and yellow/white indicates martensite. (In grayscale version of the image, darkest regions indicate ferrite, lightest regions indicate martensite, and the remaining regions indicate bainite.) **c.** SEM SE image of the material microstructure after thermo-mechanical simulation, obtained after etching the sample with 2% nital solution for 10 s. 'F' represents ferrite, 'M' represents martensite, and 'B' represents bainite

Table 5 Comparison between phase area % obtained from JMatPro® software and phase area % quantified from tint-etched micrographs using color-based threshold, for the microstructure at HAZ of GMA-welded DP980 steel

Case	Ferrite (area %)	Bainite (area %)	Martensite (area %)
Experiment (optical micrograph)	24 ± 4	44 ± 6	32 ± 5
Simulation (without scaling factor)	2.5	97.5	0
Simulation (with scaling factor)	28	46	26

Table 6 Effective macroscale properties calculated with rule of mixtures applied on properties of ferrite, bainite, and martensite phases obtained from JMatPro® software

Property	Ferrite	Bainite	Martensite	Rule of mixtures
Elastic modulus	210 GPa	210 GPa	210 GPa	210 GPa
Poisson's ratio	0.29	0.29	0.29	0.29
Specific heat capacity	448 $\mathrm{Jkg^{-1}\,K^{-1}}$	449 $\mathrm{Jkg^{-1}\,K^{-1}}$	448 $\mathrm{Jkg^{-1}\,K^{-1}}$	448 $\mathrm{Jkg^{-1}\,K^{-1}}$
Thermal expansion coefficient	$1.3 \times 10^{-5}\,\mathrm{K^{-1}}$	$1.3 \times 10^{-5}\,\mathrm{K^{-1}}$	$1.3 \times 10^{-5}\,\mathrm{K^{-1}}$	$1.3 \times 10^{-5}\,\mathrm{K^{-1}}$
Thermal conductivity	31.4 $\mathrm{Wm^{-1}\,K^{-1}}$	33.7 $\mathrm{Wm^{-1}\,K^{-1}}$	31.4 $\mathrm{Wm^{-1}\,K^{-1}}$	32.46 $\mathrm{Wm^{-1}\,K^{-1}}$
Density	7818 $\mathrm{kgm^{-3}}$	7818 $\mathrm{kgm^{-3}}$	7808 $\mathrm{kgm^{-3}}$	7815 $\mathrm{kgm^{-3}}$

Phase-Field Simulation of Microstructure Evolution at HAZ of DP980 GMA Weld

Figure 5a shows the initial microstructure used for phase-field simulation. The microstructure was generated synthetically using Voronoi Tessellation implemented in Micress® software [38]. The microstructure was generated in such a way that it represents experimentally measured average austenite grain size of 5.4 μm at austenitization temperature of 1193 K after holding at this temperature for 300 s. The time–temperature profile shown in Fig. 4a was used as an input to the software. Figure 5b shows the phase-field simulated microstructure with austenite, ferrite, and bainite at 673 K after the bainite transformation was completed. The darkest colored regions represent austenite, and the lightest colored regions represent bainite. The intermediate colored regions represent ferrite. The remaining austenite in this microstructure was assumed to have transformed to martensite upon reaching room temperature. Table 7 shows the comparison of phase fraction of ferrite, bainite, and martensite between the phase-field simulation and experiment, measured from optical micrograph. The ferrite and bainite phase fraction in the simulated microstructure agreed well with the experiments.

Table 7 Comparison between phase-field simulated phase area % and phase area % quantified from tint-etched micrographs

Case	Ferrite (area %)	Bainite (area %)	Martensite (area %)
Experiment (optical micrograph)	24 ± 4	44 ± 6	32 ± 5
Phase-field simulation	26	49	25

Figure 5d represents the carbon distribution map for the phase-field simulated microstructure. The map shows the

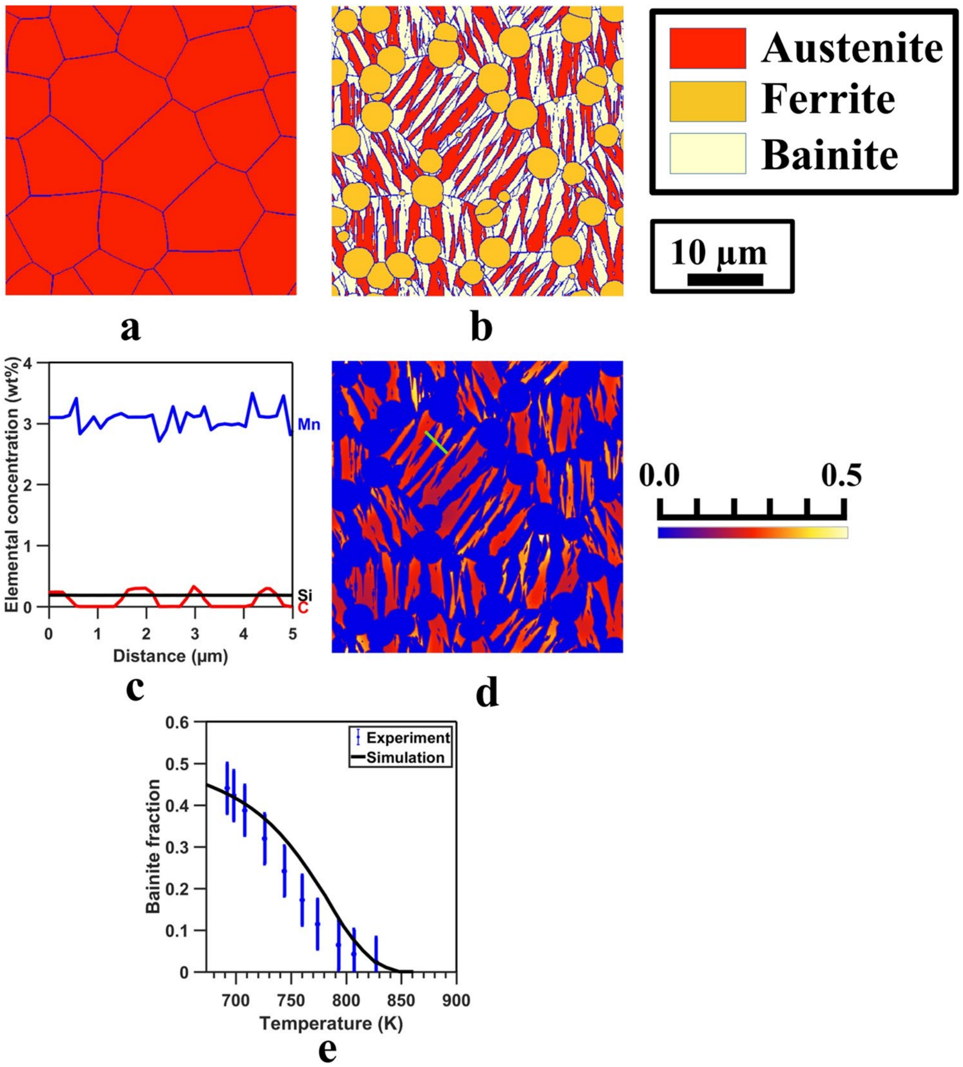

Fig. 5 Phase-field simulation of microstructure evolution at HAZ of GMA-welded DP980 steel: **a.** Initial microstructure at 1193 K, containing 18 austenite grains. **b.** Final microstructure after cooling to 673 K. Microstructure contains ferrite, bainite, and austenite. **c.** Virtual EDX line scan showing the elemental segregation across bainite sheaves at 673 K. **d.** Carbon concentration map showing the distribution of carbon in the microstructure at 673 K and the line along which Virtual EDX line scan was taken. **e.** Comparison of bainite phase fraction evolution between phase-field simulation and experiment. The phase fraction evolution from experiment was obtained with dilatometry test and microstructure analysis

distribution of carbon in the microstructure at 673 K. There were some regions in the microstructure (such as between the bainite sheaves) where higher carbon concentration was present. This higher concentration of carbon occurred due to the rejection of carbon from ferrite and bainite to surrounding austenite phase, during their growth. Regions with higher density of bainite showed higher segregation of carbon. This in turn could affect the mechanical property of martensite that forms in this region [30]. A Virtual EDX line scan was taken on the phase-field simulated microstructure to study the elemental segregation of all the elements. Figure 5c shows variation in elemental concentration in weight % with distance along the Virtual EDX line scan for the elements Mn, Si, and C. Among the alloying elements, Si and Mn—Mn showed higher segregation, whereas Si showed only minor segregation between bainite and austenite. For Mn, the segregation occurred mainly at the grain boundary. Due to the segregation occurring at the grain boundary, Mn concentration lowered within the bainite sheaf and increased in the surrounding austenite. This was not observed in the case of Si. This observation aligns closely with the literature, where higher segregation was observed for Mn, compared to that of Si in multi-component steel [39]. Figure 5e shows the comparison of bainite phase fraction evolution between phase-field simulation and experiment. The phase fraction evolution from experiment was obtained with dilatometry test and microstructure analysis. The agreement between simulated phase transformation kinetics and the experiments is satisfactory. The average ferrite grain size at room temperature was measured from experiments using linear intercept method (ASTM Standard E 112) and was found to be 2.23 ± 0.4 µm. This agreed well with the simulated average ferrite grain size which was measured to be 2.86 ± 0.3 µm.

Virtual Test Simulation and Experimental Validation

The phase-field simulated microstructure shown in Fig. 5b was used as an input for the finite element-based virtual test simulation at room temperature. The remaining austenite in this microstructure was assumed to have completely transformed to martensite. Figure 6a shows the von Mises stress distribution in MPa, in the microstructure at 2% strain during the virtual uniaxial tensile test. The ferrite and bainite being relatively softer phases compared to martensite have lesser stress values, compared to martensite. Figure 6b shows the macroscale effective flow curve obtained from the virtual test obtained by plotting the von Mises stress against effective plastic strain, compared with that obtained from experiments. There was a good agreement between the simulated and experimental flow curves. Better agreement with experimental data could be possible by performing a 3D simulation which would be computationally expensive.

Asymptotic Homogenization

The phase-field simulated microstructure shown in Fig. 5b was meshed with hexahedral elements for performing asymptotic homogenization. Table 8 shows the effective macroscale thermo-elastic properties at room temperature, obtained from phase-field simulated microstructure after performing asymptotic homogenization. The random orientation assigned to the grains during phase-field simulation was used as a microstructure input for the asymptotic homogenization. These effective properties can be used as

Table 8 Effective macroscale thermo-elastic properties at room temperature, obtained from phase-field simulated microstructure with the help of asymptotic homogenization

Property	Value
Elastic modulus	210 GPa
Poisson's ratio	0.29
Specific heat capacity	$450\,\mathrm{Jkg^{-1}K^{-1}}$
Thermal expansion coefficient	$1.3 \times 10^{-5}\mathrm{K^{-1}}$
Thermal conductivity	$33.2\,\mathrm{Wm^{-1}K^{-1}}$
Density	$7810\,\mathrm{kgm^{-3}}$

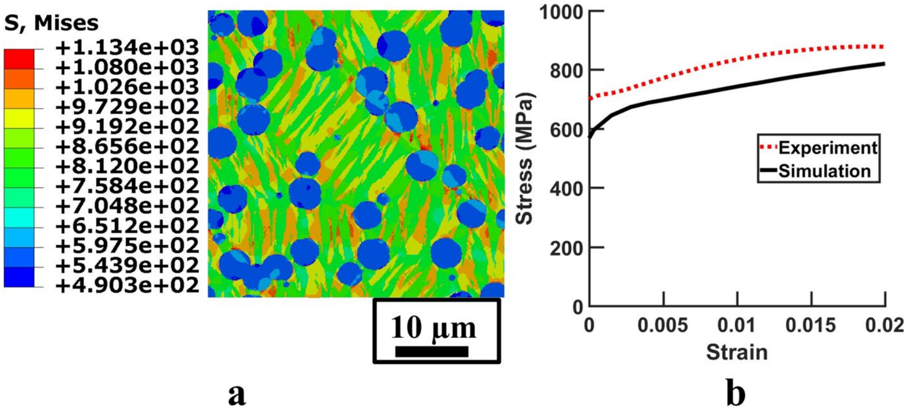

Fig. 6 Uniaxial tensile test: **a.** von Mises stress distribution (in MPa) in the simulated microstructure, at 2% strain, during the virtual uniaxial tensile test. **b.** Comparison of simulated and experimental flow curves. Variation of true stress with true strain obtained from experiment was plotted against the variation of von Mises stress with equivalent plastic strain obtained from virtual test simulation

an input for macroscale FEM simulation of processes like welding.

ICME Methodology

Figure 7 shows the ICME methodology adopted in the current work. Simulations were used to perform careful experiments, and the obtained experimental data were used for validation of simulations at various length scales. At the macroscale, an experimentally validated FEM simulation of welding was used to obtain the time–temperature profile at a point in the HAZ of GMA-welded DP980 steel. Thermomechanical simulation and microstructure characterization were used to study the microstructure evolution at this point in HAZ during cooling. The ICME workflow consists of two stages. In the first stage, semiempirical models implemented in JMatPro® software were used for the prediction of microstructure phase fraction at a point in the HAZ after cooling. The phase fractions were validated with the help of experimental data, and a scaling factor was introduced to account for the deviations. Linear rule of mixture was used for obtaining the effective macroscale properties from the phase fractions and properties of individual phases, obtained from semiempirical models implemented in JMatPro® software. In the second stage of the workflow, at the microscale, phase-field simulations were used to simulate the microstructure evolution for the obtained time–temperature profile at HAZ of a DP980 steel GMA weld. Asymptotic homogenization and virtual test were used for obtaining the effective macroscale properties from the simulated microstructure. Unlike stage 1, the effective properties in stage 2 take into account the morphology and orientation information of DP 980 steel microstructure. With the help of this ICME workflow, the effective macroscale properties were obtained for a point in the HAZ of GMA-welded DP980 steel. The dotted arrow line in Fig. 7 represents the workflow looping that could ultimately lead to a full dataset for macroscale FEM simulation of welding by considering all possible thermal cycles for the complete weld regions. Such a dataset of effective properties has the capability of considering the effect of material microstructure while providing effective material properties for macroscale FEM simulation of welding process.

Conclusions

An ICME-based workflow in two stages with an integrated utilization of simulation tools and experimental methods was developed for studying the microstructure and property evolution at a point in the HAZ of gas metal arc (GMA)-welded DP980 steel. Simultaneous transformation of austenite to

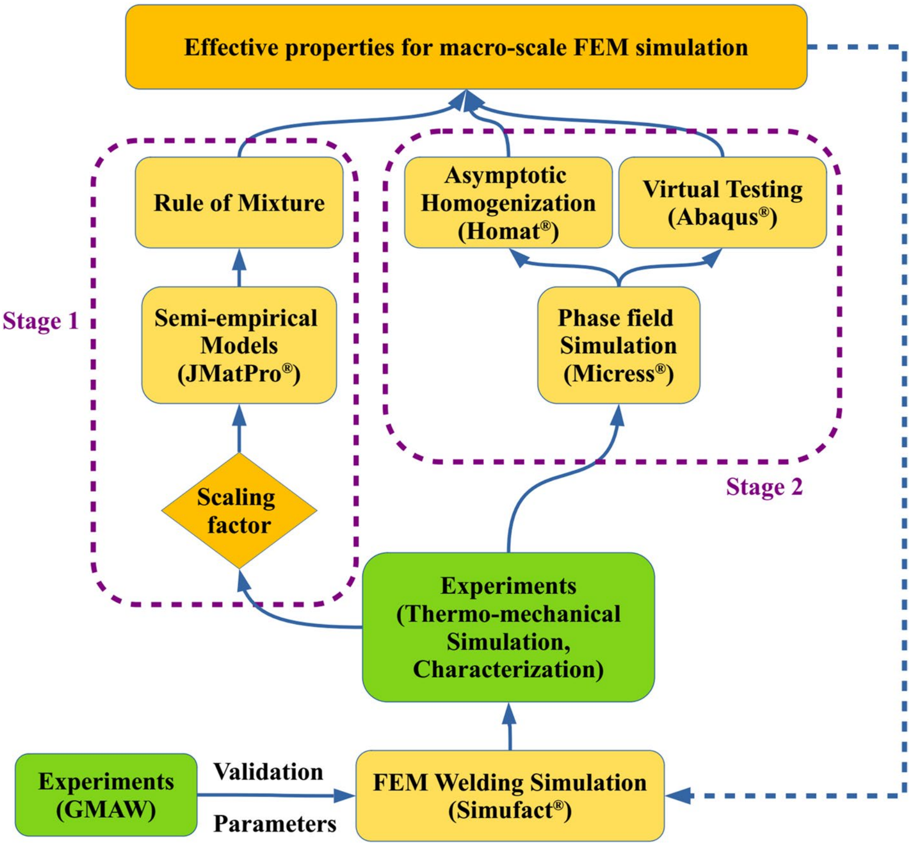

Fig. 7 ICME workflow used in GMA welding of DP980 steel for obtaining the effective macroscale properties for a point in the HAZ of GMA-welded DP980 steel. Dotted arrow line represents the possible looping for repeating the workflow to build a full dataset of effective macroscale for all possible thermal cycles in the complete weld regions

ferrite and austenite to bainite occurring during cooling at HAZ was simulated with phase-field modeling and with semiempirical models implemented in JMatPro® software. The bainite formation kinetics obtained from phase-field simulation agreed well with experiments with a maximum deviation of 4%. The flow curve obtained from virtual test agreed well with experiments with a maximum deviation of 110 MPa, which was due to the usage of 2D RVE for the Virtual test. With the proposed ICME workflow, the macroscale effective properties for a single point at HAZ of GMA-welded DP980 steel were obtained. On looping the workflow, a complete dataset of effective properties for the complete weld regions with microstructure morphology and orientation consideration could be obtained.

Acknowledgements The authors would like to acknowledge the financial support from the Indo-German Science and Technology Centre (IGSTC), New Delhi, India, for the project ‘DP-Forge’ and Center for Excellence in Iron and Steel Technology (CoExiST), IIT Madras. The authors would also like to acknowledge JSW Steel, Karnataka, India, for providing the material for research.

Data Availability The data that support the results of this study are available from the corresponding author upon reasonable request.

Compliance with Ethical Standards

Conflict of interest The authors declare that they have no known competing financial interests or personal relationships that could have appeared to influence the work reported in this paper.

References

1. Schmitz GJ, Engstrom A, Bernhardt R, Prahl U, Adam L, Seyfarth J, Apel M, de Saracibar CA, Korzhavyi P, Ågren J, Patzak B (2016) Software solutions for ICME. J Miner Metals Mater Soc 68:70–76
2. Allison J, Backman D, Christodoulou L (2016) Integrated computational materials engineering: a new paradigm for the global materials profession. J Miner Metals Mater Soc 58:25–27. https://doi.org/10.1007/s11837-006-0223-5
3. Helm D, Butz A, Raabe D, Gumbsch P (2011) Microstructure-based description of the deformation of metals: theory and application. J Miner Metals Mater Soc 63:26–33
4. John DM, Farivar H, Rothenbucher G, Kumar R, Zagade P, Khan D, Babu A, Gautham BP, Bernhardt R, Phanikumar G, Prahl U (2017) An attempt to integrate software tools at microscale and above towards an ICME approach for heat treatment of a DP steel gear with reduced distortion. Miner Metals Mater Ser Part F 4:3–13. https://doi.org/10.1007/978-3-319-57864-4_1
5. Deepu MJ, Farivar H, Prahl U, Phanikumar G (2017) Microstructure based simulations for prediction of flow curves and selection of process parameters for inter-critical annealing in DP steel. IOP Conf Ser Mater Sci Eng 192:012010. https://doi.org/10.1088/1757-899X/192/1/012010
6. Rahul MR, Phanikumar G (2015) Correlation of microstructure with HAZ welding cycles simulated in Ti-15-3 alloy using Gleeble 3800 and SYSWELD. Mater Perform Charact 4:381–398
7. Steinbach I (2009) Phase-field models in materials science. Modell Simul Mater Sci Eng 17:073001. https://doi.org/10.1088/0965-0393/17/7/073001
8. DeWitt S, Thornton K (2018) Phase field modeling of microstructural evolution. In: Shin D, Saal J (eds) Computational materials system design. Springer, Cham. https://doi.org/10.1007/978-3-319-68280-8_4
9. Boettinger WJ, Warren JA, Beckermann C, Karma A (2002) Phase-field simulation of solidification. Ann Rev Mater Res 32:163–194
10. Thornton K, Ågren J, Voorhees PW (2003) Modelling the evolution of phase boundaries in solids at the meso- and nano-scales. Acta Mater 51:5675–5710
11. Mecozzi MG, Sietsma J, Van Der Zwaag S, Apel M, Schaffnit P, Steinbach I (2005) Analysis of the $\gamma \rightarrow \alpha$ transformation in a C-Mn steel by phase-field modeling. Metall Mater Trans A 36:2327–2340
12. Mecozzi MG, Sietsma J, Van Der Zwaag S (2005) Phase field modelling of the interfacial condition at the moving interphase during the $\gamma \rightarrow \alpha$ transformation in C-Mn steels. Comput Mater Sci 34:290–297
13. Mecozzi MG, Sietsma J, Van Der Zwaag S (2006) Analysis of $\gamma \rightarrow \alpha$ transformation in a Nb micro-alloyed C-Mn steel by phase field modelling. Acta Mater 54:1431–1440
14. Militzer M, Mecozzi MG, Sietsma J, van der Zwaag S (2006) Three-dimensional phase field modelling of the austenite-to-ferrite transformation. Acta Mater 54:3961–3972
15. Mecozzi MG, Militzer M, Sietsma J, Zwaag S (2008) The role of nucleation behavior in phase-field simulations of the austenite to ferrite transformation. Metall Mater Trans A 39:1237–1247
16. Zhu B, Militzer M (2014) Phase-field modeling for intercritical annealing of a dual-phase steel. Metall Mater Trans A 46:1073–1084
17. Zhu B, Chen H, Militzer M (2015) Phase-field modeling of cyclic phase transformations in low-carbon steels. Comput Mater Sci 108:333–341
18. Mukherjee K, Prahl U, Bleck W, Reisgen U, Schleser M, Abdurakhmanov A (2010) Characterization and modelling techniques for gas metal arc welding of DP 600 sheet steels. Materialwiss Werkstofftech 41:972–983
19. Arif TT, Qin RS (2014) A phase-field model for the formation of martensite and bainite. Adv Mater Res 922:31–36
20. Bhattacharya A, Upadhyay CS, Sangal S (2015) Phase-field model for mixed-mode of growth applied to austenite to ferrite transformation. Metall Mater Trans A 46:926–936
21. Düsing M, Mahnken R (2016) A thermodynamic framework for coupled multiphase Ginzburg-Landau/Cahn-Hilliard systems for simulation of lower bainitic transformation. Arch Appl Mech 86:1947–1964
22. Ramazani A, Li Y, Mukherjee K, Prahl U, Bleck W, Abdurakhmanov A, Schleser M, Reisgen U (2013) Microstructure evolution simulation in hot rolled DP600 steel during gas metal arc welding. Comput Mater Sci 68:107–116
23. Toloui M, Militzer M (2018) Phase field modeling of the simultaneous formation of bainite and ferrite in TRIP steel. Acta Mater 144:786–800
24. Laschet G (2002) Homogenization of the thermal properties of transpiration cooled multi-layer plates. Comput Methods Appl Mech Eng 191:4535–4554
25. Laschet G (2004) Homogenization of the fluid flow and heat transfer in transpiration cooled multi-layer plates. J Comput Appl Math 168:277–288
26. Laschet G, Apel M (2010) Thermo-elastic homogenization of 3-D steel microstructure simulated by the phase-field method. Steel Res Int 81:637–643

27. Laschet G, Shukla M, Henke T, Fayek P, Bambach M, Prahl U (2014) Impact of the microstructure on the U-O forming simulations of a ferrite-pearlite pipeline tube. Steel Res Int 85:1083–1098
28. Ramazani A, Mukherjee K, Quade H, Prahl U, Bleck W (2013) Correlation between 2D and 3D flow curve modelling of DP steels using a microstructure-based RVE approach. Mater Sci Eng, A 560:129–139
29. Farivar H, Rothenbucher G, Prahl U, Bernhardt R (2017) ICME-based process and alloy design for vacuum carburized steel components with high potential of reduced distortion. Miner Metals Mater Ser Part F 4:133–144
30. Farivar H, Deepu MJ, Hans M, Phanikumar G, Bleck W, Prahl U (2019) Influence of post-carburizing heat treatment on the core microstructural evolution and the resulting mechanical properties in case-hardened steel components. Mater Sci Eng A 744:778–789
31. Santofimia MJ, Zhao L, Sietsma J (2011) Overview of mechanisms involved during the quenching and partitioning process in steels. Metall Mater Trans A 42:3620–3626
32. ImageJ (2020). https://imagej.nih.gov/ij/index.html. Accessed 26 April 2020
33. Rezayat H, Ghassemi-Armaki H, Bhat SP, Sriram S, Babu SS (2019) Constitutive properties and plastic instabilities in the heat-affected zones of advanced high-strength steel spot welds. J Mater Sci 54:5825–5843
34. Simufact Welding (2020). https://www.simufact.com/simufactwelding-welding-simulation.html. Accessed 30 May 2020
35. Goldak J, Chakravarti A, Bibby M (1984) A new finite element model for welding heat sources. Metall Trans B 15:299–305
36. JMatPro (2020). https://www.sentesoftware.co.uk/jmatpro. Accessed 11 May 2020
37. Mecozzi MG, Eiken J, Santofimia MJ, Sietsma J (2016) Phase field modelling of microstructural evolution during the quenching and partitioning treatment in low-alloy steels. Comput Mater Sci 112:245–256
38. Micress (2020). https://micress.rwth-aachen.de/. Accessed 26 April 2020
39. Goulas C, Mecozzi MG, Sietsma J (2016) Bainite formation in medium-carbon low-silicon spring steels accounting for chemical segregation. Metall Mater Trans A 47:3077–3087